PHYSICAL REVIEW B **106**, 085102 (2022)

Coexistence of multifold and multidimensional topological phonons in $KMgBO_3$

P. C. Sreeparvathy,[1] Chiranjit Mondal,[1,2] Chanchal K. Barman,[1,3] and Aftab Alam[1,*]
[1]Department of Physics, Indian Institute of Technology Bombay, Powai, Mumbai 400076, India
[2]Center for Correlated Electron Systems, Institute for Basic Science (IBS), Seoul 08826, Korea
[3]Department of Physics, Sungkyunkwan University, Suwon 16419, Republic of Korea

(Received 23 November 2021; revised 10 June 2022; accepted 22 July 2022; published 1 August 2022)

Topological interpretations of phonons facilitate a platform for unique concepts in phonon physics. Though there are ubiquitous reports on topological electronic excitations, the same for phonons is extremely limited. Here, we propose a candidate material, $KMgBO_3$, which showcases the coexistence of several multifold and multidimensional topological phonon excitations, which are protected by spatial and nonspatial symmetries. This includes zero-dimensional double, triple, and quadratic Weyl phonon nodes, one-dimensional nodal line/loops, and two-dimensional doubly degenerate nodal surface states. The nodal line/loop emerges from the spin-$\frac{1}{2}$ phonon nodes, while the two-dimensional doubly degenerate nodal surface arises from a combination of twofold screw-rotational and time-reversal symmetries. Application of strain breaks the C_3 rotational symmetry, which destroys the spin-1 double Weyl nodes but preserves other topological features. Interestingly, strain helps create two extra single Weyl nodes, which in turn preserve the total chirality. Alloying also breaks certain symmetries, destroying most of the topological phonon features in the present case. Thus, $KMgBO_3$ is a promising candidate which hosts various Weyl points, large Fermi arcs with very clean phonon spectra, and tunable topological phonon excitations, and hence is certainly worth future theoretical/experimental investigation of topological phononics.

DOI: 10.1103/PhysRevB.106.085102

I. INTRODUCTION

Topological properties of fermionic states enforced by spatial and nonspatial symmetries have been ubiquitously explored in the literature [1–7]. The same for bosons (photons, phonons), however, has started only recently [8–10] and there are only limited studies along these lines. The concept of chiral phonons is further extended to materials with nonsymmorphic crystalline symmetry, which unlocks applications in the THz frequency range [11–13]. In addition, topological phonons also find applications in unconventional heat transfer, electron-phonon coupling, and phonon diodes [10,12,14]. The advantage of topological bosons over fermions is the possibility of probing topological states in any frequency range using experimental techniques unlike fermionic states, where this is mostly possible only near the Fermi level (E_F). In line with electronic states, topological phonons also show anomalous transport behavior, such as the anomalous phonon Hall effect [15–17]. Over the years, diverse quasiparticle excitations have emerged as a consequence of different band crossings which can host nonzero topological Chern numbers. For instance, conventional spin-$\frac{1}{2}$ Weyl fermions possess Chern number ±1. Moreover, unconventional chiral particles with a Chern number greater than unity have also been realized in crystalline systems. Threefold spin-1 and fourfold charge-2 Dirac fermions are examples of such higher Chern number quasiparticles [18–20]. These multifold band crossings yield a zero-dimensional (0D) point degeneracy in momentum space [21]. There exist other types of topological band crossings such as nodal lines/loops and nodal surfaces which induce one-dimensional(1D) and two-dimensional (2D) degeneracy, respectively [22]. A proper understanding and the hunt for real materials hosting multiple topological phonons have emerged as a frontline research area due to its demand from both fundamental and application perspectives. Several 3D and 2D materials are investigated for topological phonons [23–26]. Advantages of materials with multiple topological phonon excitations (including multifold and multidimensional) can be understood/appreciated from the following special features: First, topological phonon band crossings and the associated excitations can be found in a wide frequency range (acoustic as well as optical regime). All these band crossings are equally important and play a crucial role in dictating the thermal transport of a given material, unlike the electronic band structure where the topological band crossings near the Fermi level are the key to driving the electronic transport. Second, various topological bulk phonon features induce unique surface properties such as drumheadlike surface spectra, highly dispersive spectra, large surface arcs, etc. The coexistence of these features can attract various phonon device applications. A recent study reported the enhancement of thermoelectric response due to the presence of triple-point phonons [27]. The coexistence of a few multidimensional topological phonons has been identified in some materials [28]. However, to the best of our knowledge, the coexistence of multifold and multidimensional (such as nodal points, nodal lines, and nodal surfaces) phononic quasiparticles is rarely reported in real materials.

Tuning the topological properties of material via strain/pressure/doping is a well-accepted method that

---

[*] aftab@iitb.ac.in

helps to modify the symmetry and hence the electronic structure, facilitating the onset of trivial/nontrivial topological excitations [29,30]. There have been several theoretical/experimental studies which have showcased such symmetry-mediated transitions from topological insulator to semimetal and vice versa, creation and removal of Weyl/Dirac and other kinds of topological nodes [31–33]. A similar band engineering and the associated transition can be expected for phonon quasiparticles as well.

In this paper, we present the coexistence of several topological phonon excitations in a single compound, $KMgBO_3$, which crystallises in a cubic phase. $KMgBO_3$ is an experimentally synthesized chiral compound, which has been explored for nonlinear optical properties [34,35]. Recently, we also found this compound to show interesting topological electronic properties [20]. One of the main focuses of the present paper is to investigate the topological phonon excitations and the effect of symmetry breaking on the topological properties of this material. Pristine $KMgBO_3$ has a rich phonon band dispersion, showing several topologically nontrivial multifold/multidimensional band crossings in different frequency ranges. This includes spin-1 Weyl, charge-2 Dirac, single Weyl, nodal line, nodal loop, and nodal surface states. These states are topologically protected by crystalline and time-reversal symmetries. Application of strain breaks the C_3 rotational symmetry, which removes the spin-1 double Weyl nodes but preserves the charge-2 Dirac node and nodal surface states. We have further disturbed the symmetry by doping with Rb, transforming it into a triclinic structure. Though doping preserves the total chirality, it destroys all the topological phonon features. Additionally, we have explored two other prototype compounds, $RbMgBO_3$ [36] and $CsCdBO_3$ [37], which show similar topological features.

II. COMPUTATIONAL DETAILS

We have performed density-functional theory and density-functional perturbation theory calculations to study the ground state and phonon dispersion of $KMgBO_3$ as implemented in the VIENNA AB INITIO SIMULATION PACKAGE [38,39] and PHONOPY [40]. Generalized gradient approximation by Perdew-Burke-Ernzerhof is considered to capture the effect of exchange and correlation [39]. Force constants were calculated using a $2 \times 2 \times 2$ supercell with an energy convergence of 10^{-7} eV. A tight-binding Hamiltonian was constructed using the converged force constants and further imposed with theWANNIER TOOL [41] package to investigate the topological phonon surface states, surface arc, chirality, and Berry curvature. Strain is applied by changing the lattice parameters and the atomic positions were further optimized. Irreducible representations of phonon states based on the tight-binding Hamiltonian were obtained using the IR2TB program [42]. The high-symmetry points in the bulk Brillouin zone (BZ) of $KMgBO_3$ are Γ (0,0,0), X(0.5,0,0), M(0.5,0.5,0), and R(0.5,0.5,0.5). On the (001) surface, however, the Γ point is projected as $\bar{\Gamma}$; R and M points are projected as $\bar{M}$(0.5,0.5); and the side point X is projected as $\bar{X}$ (0.5,0.0). Similarly, one can understand the (010) and (100) surfaces.

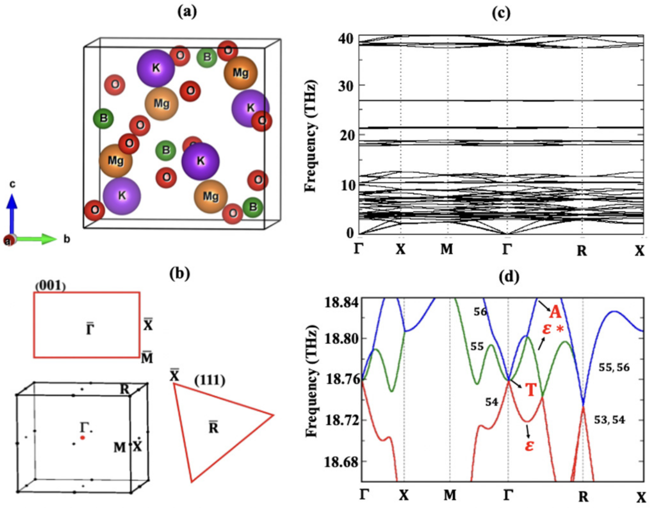

FIG. 1. For $KMgBO_3$, (a) Crystal structure [space group $P2_13$ (No. 198)]. (b) Brillouin zone (BZ) for bulk, (001), and (111) surfaces. (c) Full phonon spectra. (d) Phonon spectra in a small frequency interval, with the highlighted bands character. T, E, ε, and ε^* are the irreducible representations according to T_4 point group symmetry.

III. RESULTS AND DISCUSSION

A. Crystal structure

$KMgBO_3$ crystallizes in a cubic structure with space group $P2_13$ (No. 198) [34]. The theoretically optimized lattice parameter (6.09 Å) matches fairly well with the experiment (6.8345 Å) [34]. Figures 1(a) and 1(b) show the real-space crystal structure and bulk, (001), and (111) surface BZs. Space group No. 198 holds the tetrahedron (T_4) point-group symmetry, which provides two twofold screw rotations, $S_{2z} = \{C_{2z}|\frac{1}{2}, 0, \frac{1}{2}|\}$, $S_{2y} =\{C_{2z}|0, \frac{1}{2}, \frac{1}{2}|\}$, and one threefold rotation, $S_3= \{C^{+}_{3,111}|0,0,0\}$, as generators at the Γ point. At the R point, the generators are $S_{2x} = \{C_{2x}|\frac{1}{2}, \frac{3}{2}, 0|\}$, $S_{2y} = \{C_{2y}|0, \frac{3}{2}, \frac{1}{2}|\}$ and $S_3= \{C^{-}_{3,111}|0,0,0\}$, while at the X point, they are $S_{2y} = \{C_{2y}|0, \frac{1}{2}, \frac{1}{2}|\}$ and $S_{2z} = \{C_{2z}|\frac{1}{2}, 0, \frac{1}{2}|\}$ [43]. In addition, the space group preserves time-reversal symmetry (T). To understand further, we have examined the irreducible representations of $KMgBO_3$. According to the T_4 point group character table, a total of 12 symmetry operations are present in $KMgBO_3$ with elements E, four C_3 rotations, four $(C_3)^2$, and three C_2 rotations. The representations are named A, E, and T, where A is 1D, E is 2D, and T is 3D in nature. Corresponding characterization tables for T_4, C_3, and C_2 point groups are provided in Tables I, II, and III.

TABLE I. Characterization table for T_4 point group

T	E	$4C_3$	$4C_3^2$	$3C_2$
A	+1	+1	+1	+1
E	+1,+1	+ε,+ε*	+ε*,+ε	+1,+1
T	3	0	0	−1

TABLE II. Characterization table for C_3 point group.

C_3	E	C_3	$(C_3)^2$
A	+1	+1	+1
E	+1,+1	$+\varepsilon$,$+\varepsilon^*$	$+\varepsilon^*$,$+\varepsilon$

B. Phonon spectra

$KMgBO_3$ structure involves four formula units leading to 24 atoms in the unit cell, which generate three acoustic and 69 optical phonon modes. A phonon dispersion over a wider range of frequency (0–40 THz) is presented in Fig. 1(c). The absence of imaginary modes confirms the dynamical stability of the compound. A close inspection of bulk phonon dispersion reveals the prosperity of different natures of band crossings in different frequency ranges, yielding topological Weyl, nodal line/loop, and nodal surface states, as discussed in detail below. We have also studied the surface phonon spectra corresponding to each topological feature.

C. Double Weyl phonons

Symmetry enforced three- or fourfold band crossings can induce unconventional topological excitations such as spin-1 and charge-2 Dirac nodes [44]. A spin-1 double Weyl phonon originates from a three-band Hamiltonian while a charge-2 Dirac node originates from a four-band Hamiltonian. Let us first consider the case at the Γ point. For phonons, the square of the time-reversal symmetry operator (T) is identity (I). The generators S_{2z} and S_{2y} commute with each other at the Γ point, which can be understood by considering the transformation of lattice coordinates as a function of the twofold screws C_{2z} and C_{2y}. The transformations are $C_{2z}(x, y, z) \rightarrow (-x, -y, z)$ and $C_{2y}(x, y, z) \rightarrow (-x, y, -z)$, which define $S_{2z}^2 = 1$, $S_{2y}^2 = 1$ and $S_{2z}S_{2y} = S_{2y}S_{2z}$ [43]. The lattice coordinate transformation due to C_3 is $C_{3,111}(x, y, z) = (z, x, y)$, which shows $S_3^2 = 1$. To understand the degeneracy of bands at Γ, one needs to consider the eigenstates generated by these symmetry operators which commute with the Hamiltonian of the system, $S_{2z}|\psi> = \lambda_1|\psi>$, $S_{2y}|\psi> = \lambda_2|\psi>$, where $\lambda_1 = \pm 1$, $\lambda_2 = \pm 1$ according to $S_{2z}^2 = 1$ and $S_{2y}^2 = 1$. S_3 obeys $S_{2z}S_3 = S_3S_{2y}$ and $S_3S_{2z}S_{2y} = S_{2y}S_3$, which impose a threefold degeneracy at Γ with eigenstates $|\psi>$, $|S_3\psi>$ and $|S_3^2\psi>$, when screws are nontrivial [20]. When screws are trivial, the Γ point can hold either nondegenerate or twofold degeneracy [20]. The above symmetry discussions explain the possibility of hosting nondegenerate, doubly degenerate, and triply degenerate bands at the Γ point. To further understand the intrinsic feature of spin-1 Weyl type-band crossings, we have analyzed the irreducible representations of these three bands: 54–56 [which are involved in the formation of spin-1 Weyl as mentioned in Fig. 1(d)] at the Γ point. These three bands are degenerate at the Γ point and the irreducible representation of these three overlapping bands at Γ is Γ_4 from the table (see Table I), which is the element T. A small shift from the Γ along the R and M points [see Fig. 1(d)] splits the triply degenerate bands to nondegenerate bands with different symmetry and irreducible representations. To verify that, we have taken a point along the Γ-R direction [say (0.16667, 0.1667, 0.1667) units of $2\pi/a$], the symmetry of this point is C_3 and E. The irreducible representations of these three bands, according to the C_3 character table, are the combination of ε, ε^*, and A. Two screws S_{2x} and S_{2y} anticommute with each other at the R point, and S_{2x}^2 = -1, $S_{2y}^2 = -1$. This induces a twofold degenerate state (with eigenvalue ±i) at the R point. Further, the combination of threefold rotation S_3 and twofold screws create two more distinct states, enabling a fourfold charge-2 Dirac point with chirality −2, −2, +2, and +2. Further symmetry-related details can be found in our previous paper [20] performed for electronic excitation. Figure 1(d) displays the phonon dispersion in a smaller frequency range where a threefold spin-1 Weyl point (at Γ) and a fourfold charge-2 Dirac point (at R) are observed. At Γ point, near 18.76 THz, three bands (band numbers 54–56) cross degenerately, with Chern number −2 (for band 54), 0 (for 55), and +2 (for 56). At the R point, near 18.73 THz, a fourfold degenerate band crossing arises which involve bands 53–56 [see Fig. 1(d)]. This fourfold unconventional Dirac-like node can be seen as a combination of two identical spin-$\frac{1}{2}$ Weyl phonons, with a net topological charge of 2 [44].

TABLE III. Characterisation table for C_2 point group.

C_2	E	C_2
A	+1	+1
B	+1	−1

Surface states of the double Weyl phonons are examined on (001) and (111) surfaces. Figures 2(a) and 2(c) show the (001) surface state corresponding to the spin-1 Weyl point and charge-2 Dirac point projected on $\bar{\Gamma}$ and $\bar{M}$ points, respectively. Two linearly dispersed and one parabolic surface state can be seen at the $\bar{\Gamma}$ point, which originated from three bulk bands with chirality −2, 0, 2, while a highly linearised surface state is observed at $\bar{M}$ point, which represents the charge-2 Dirac point. Since these two nodes at $\bar{\Gamma}$ and $\bar{M}$ possess opposite chirality, one can expect a surface arc connecting these two points. A surface arc simulated at 18.76 THz is shown in Fig. 2(b), which indirectly connects $\bar{\Gamma}$ and $\bar{M}$ points. Figure 2(d) shows the surface arc projected at a slightly lower frequency (18.73 THz), which directly connects the two points, with a long diagonal. Such large surface arcs are much easier to probe experimentally, as reported earlier for other topological phonon materials [11]. Simulated Berry curvature at the Γ point (for chirality −2) in the k_x-k_y plane is shown in Fig. 2(e), clearly confirming the flow of Berry flux from the Γ point. Further, the analysis of the (111) surface shows the presence of a charge-2 Dirac node, as shown in Fig. 2(f). We have also examined the phonon mode displacements at the Γ point originating from bands 54–56 and at the R point originating from bands 53–56. At both high-symmetry points, the elements O and B contribute maximally as compared to the other two elements. Figure 3 shows these phonon-mode displacements.

D. Single Weyl phonons

Pristine $KMgBO_3$ also hosts two types of spin-$\frac{1}{2}$ topological states: (1) 0D Weyl points and (2) 1D nodal lines/nodal

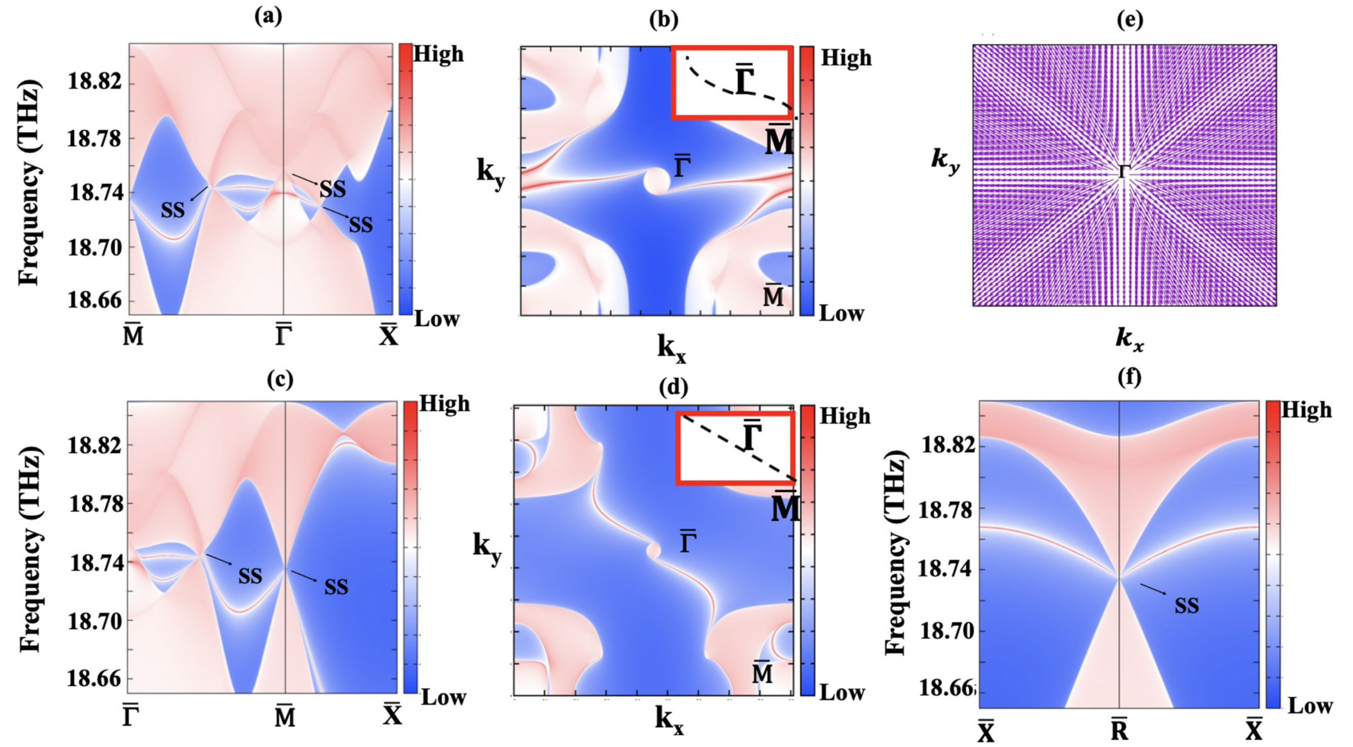

FIG. 2. For $KMgBO_3$: (a), (c) Surface state around $\bar{\Gamma}$ and $\bar{M}$ points on (001) surface, corresponding to the spin-1 Weyl node and charge-2 Dirac node, respectively. (b), (d) Surface arc at 18.76 THz and 18.73 THz between $\bar{\Gamma}$ and $\bar{M}$ points. (e) Berry flux around Γ point. (f) Surface states of charge-2 Dirac point on (111) surface. SS stands for surface states

rings. First, let us discuss the single Weyl point. Weyl nodes can be formed by breaking either the time-reversal symmetry or the inversion symmetry. In the present case, it arises from the noncentrosymmetric nature of the$KMgBO_3$ structure. Weyl nodes can be further classified into type I and type II, according to the nature of the band crossings [45–47]. In $KMgBO_3$ phonon spectra, both types of Weyl nodes are observed, as shown in Figs. 4(a) and 4(b). The Type-I Weyl point is observed in the frequency range 18.71–18.74 THz (formed by the crossing of bands 54 and 55). While, type II is observed along the Γ-R line in the frequency range 6.76–6.84 THz (formed by the crossing of bands 28 and 29). The surface states for both type-I and type-II Weyl points on the (001) surface are presented in Figs. 4(c) and 4(d)). Clearly, a highly linearized surface state with surface arc is visible for type I, while a tilted one for type II. To understand the irreducible representation of the single Weyl point, we have selected a Weyl point originating from the band numbers 54 and 55 [see Fig. 4(a)]. The coordinate of the selected Weyl point is (0.22619, 0.22619, 0.22619). To illustrate the twofold band crossing at this point, we have chosen two other nearby points, namely, K_1 and K_2 located at (0.166667 0.166667 0.166667) and (0.333333 0.333333 0.333333) respectively. Our target Weyl point is present in between these two points. The irreducible representation of bands 54 and 55 at the K_1 point are ε and ε^*, while that of bands 54 and 55 at the K_2 point are ε^* and ε, respectively, which clearly indicates the twofold band crossing in between K_1 and K_2. $KMgBO_3$ hosts several other Weyl points at different frequency ranges. A few of them originating from the bands 28, 29, 54, and 55 are summarized in Table IV.

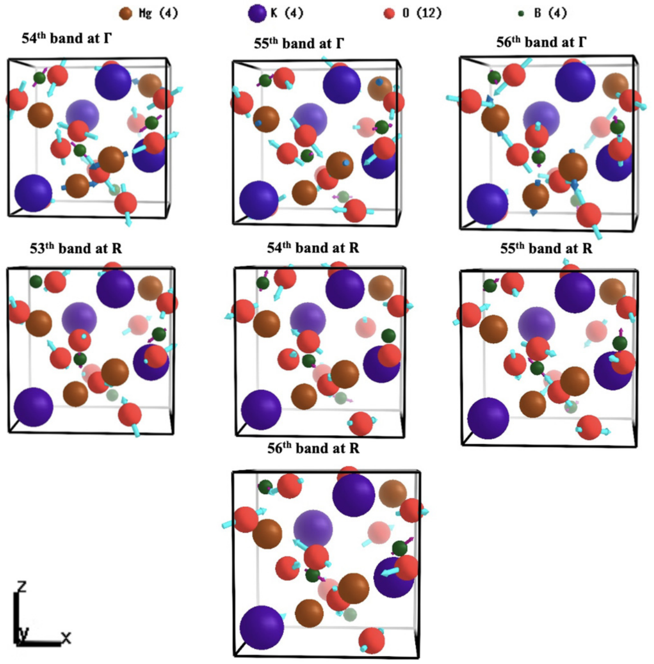

FIG. 3. For $KMgBO_3$, the phonon modes at Γ and R high-symmetry points for spin-1 Weyl and charge-2 Dirac point.

Next, we will discuss two other types of spin-$\frac{1}{2}$ topological nodal points. The presence of more than one nodal point at the small frequency limit with different momentum forms a

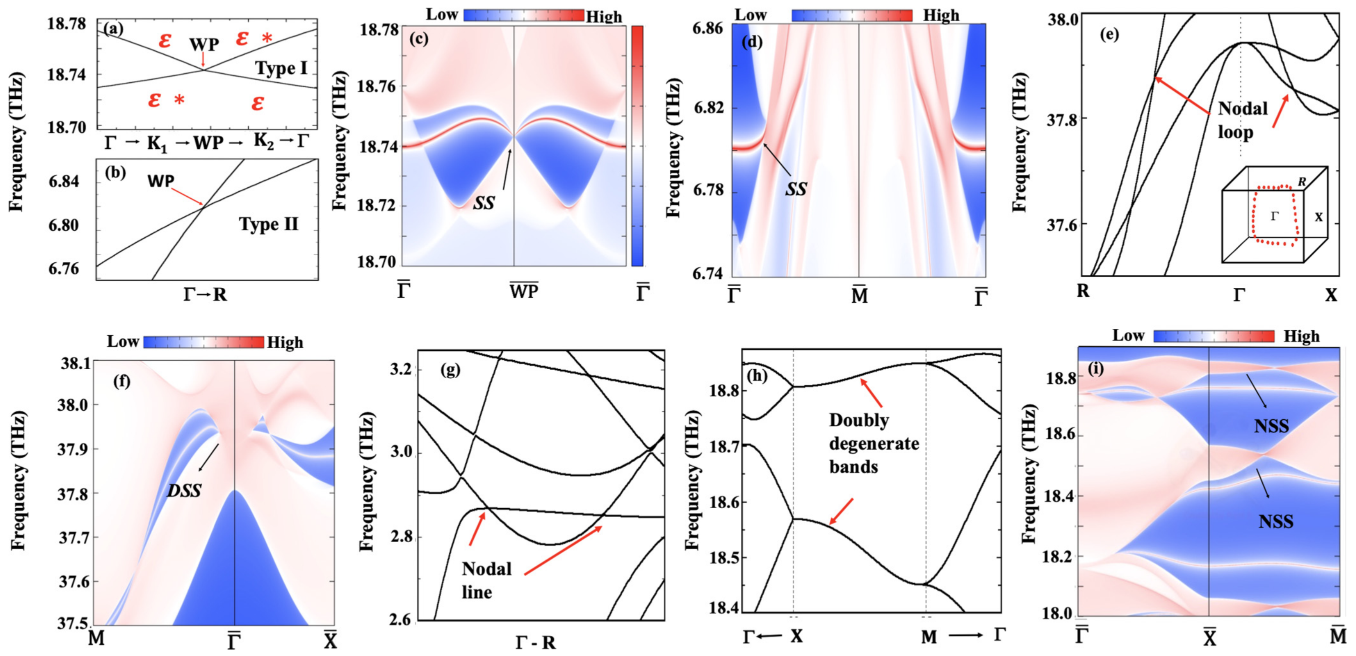

FIG. 4. For KMgBO$_3$, the phonon bands along (a) Γ-*X* and (b) Γ-*R*, showing type-I and type II Weyl crossings, respectively. ε, ε^* are the irreducible representations according to T_4 point-group symmetry. Phonon surface spectra on (001) surface corresponding to (c) type-I and (d) type-II Weyl nodes. (e) Phonon dispersion along *R*-Γ-*X* confirming a nodal loop behavior (inset figure shows the shape of the nodal loop). (f) Drumheadlike surface state on (001) surface corresponding to the nodal loop shown above. Phonon dispersion (g) along Γ-*R*, confirming a nodal line behavior (h) along *X*-*M* showing the doubly degenerate bands. (i) Surface spectra due to the doubly degenerate bands. The notations SS, DSS, and NSS stand for the surface states, drumheadlike surface states, and nodal surface states, respectively.

1D nodal line/looplike band crossing. Figure 4(e) shows one such example where two nodal points are observed along two different high-symmetry lines (Γ-*X* and Γ-*R*) within a small frequency interval. This causes the formation of a nodal loop in the tilted plane and this loop is protected by C_3 symmetry. A drumheadlike surface originating due to the nodal loop around the $\bar{\Gamma}$ point is shown in Fig. 4(f). A similar feature is observed in carbon allotrope [48]. Additionally, the phonon dispersion along Γ-*R* shows two nodal points at the same frequency resulting in a nodal line behavior [see Fig. 4(g)].

E. Nodal surface

Higher-dimensional band degeneracy has been theoretically predicted [49] and experimentally realized in recently [50]. There are a few symmetry-mediated conditions that impose such high-dimensional band degeneracy [51]. The bands along X-*M* and *X*-*R* aligned in the $k_x = \pi$ plane provide a minimum of double degeneracy due to the above condition [24,49]. Figure 4(h) shows the double degenerate band along *X*-*M*. Similarly, a doubly degenerate phonon band can be seen in $k_{y,z} = \pi$ planes. It is evident from the figure that these doubly degenerate bands are well separated and hence can be easily realized experimentally. Figure 4(i) shows the corresponding surface state, which is mostly flat with a low spread in frequency range, enabling KMgBO$_3$ to be a promising candidate for an ideal nodal surface. Similarly, one can observe a nodal surface on the other two surfaces. A combined visual of these nodal surfaces create a nodal cube around the BZ center. This is a unique surface feature of KMgBO$_3$ which stands out in comparison to other reported topological nodal surface materials [52]. To understand the irreducible representation of the bulk band origin of the nodal surface, we selected bands 53 and 54 and observed that all the points on the k_i=0.5 plane is at least doubly degenerate. The high-symmetry paths, such as *X-M, M-R, R-X,* etc., show a minimum of doubly degenerate bands and cause the formation of nodal surface states.

F. Strain effects

Both uniaxial (along *c* axis) and biaxial (along *a* and *b* axes) compressive and tensile strains are applied on KMgBO$_3$

TABLE IV. Coordinates, chirality, and frequency of Type-I Weyl points originating from bands 54, 55, 28, and 29.

Band number	Coordinates of Weyl points	Chirality	Number of points in the nearby positions	Frequency (THz)
28,29	(0.43690, 0.43690, 0.43690)	+1	8	7.05
28,29	(0.37387, −0.33265, 0.0000)	−1	8	6.95
54,55	(0.16798, 0.0000, 0.30107)	+1	8	18.73
54,55	(0.22619, −0.22619, −0.22619)	−1	8	18.74

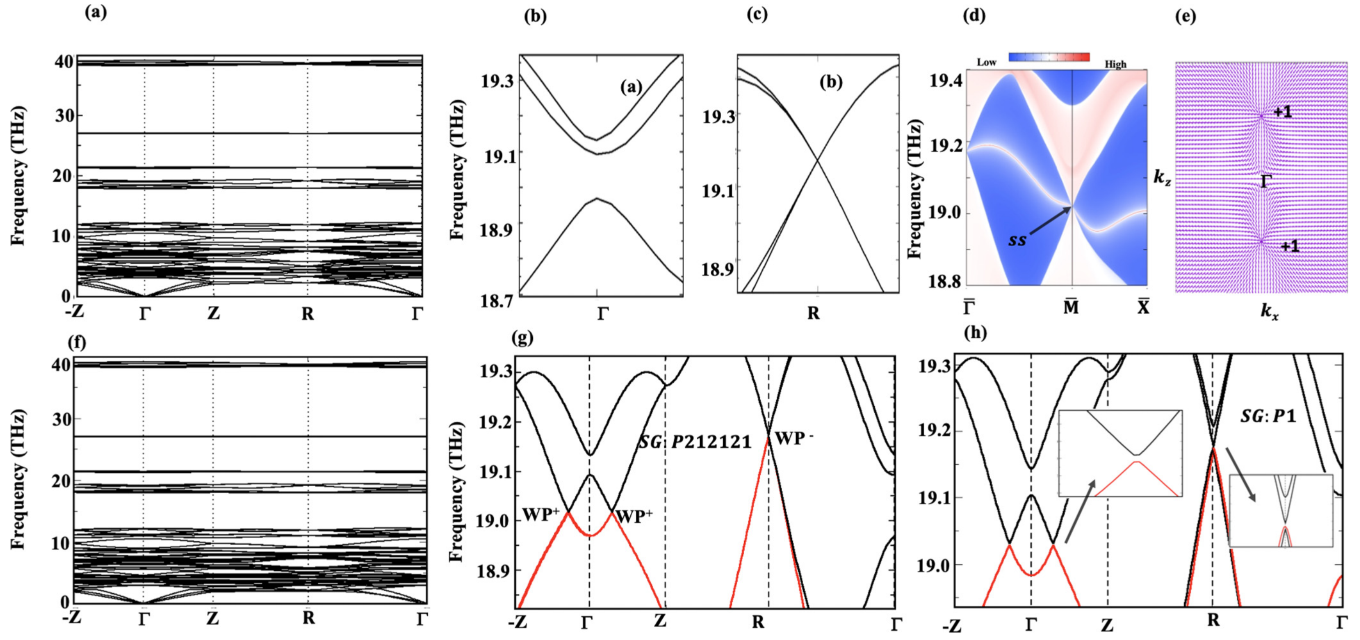

FIG. 5. For $KMgBO_3$ under 3% compressive strain: (a) Full phonon spectra and phonon spectra (b) around Γ point and (c) R point. (d) Surface state corresponding to charge-2 Dirac node at R point. (e) Berry curvature at two Weyl points on k_x-k_z plane. (f) Full phonon dispersion of Rb-substituted $KMgBO_3$. (g) Zoomed-in view of phonon dispersion in strained state (space group $P2_12_12_1$), representing the charge-2 Dirac point at R (with chirality -2) and two Weyl nodes (with chirality $+1$) along $(-Z)$ $-\Gamma$-Z. (h) Zoomed-in view of phonon dispersion of Rb-substituted $KMgBO_3$ (space group $P1$), representing the removal of charge-2 Dirac point at R and the Weyl nodes along $(-Z)$ $-\Gamma$-Z direction.

to illustrate the effect of symmetry breaking on topological phonon excitations. Such strain breaks the cubic symmetry and transforms the structure to an orthorhombic space group $P2_12_12_1$ (No. 19), which lacks threefold C_3 rotational symmetry [43]. Space group $P2_12_12_1$ has deltahedron type (D_2^4) point group involving three twofold screw rotation symmetries. At the Γ point, the generators are $S_{2z} = \{C_{2z}|\frac{1}{2}|, 0, \frac{1}{2}|\}$ and $S_{2y} = \{C_{2z}|\frac{1}{2}|, \frac{1}{2}, 0|\}$. These two satisfy the commutation relation at this point $[S_{2y}, S_{2z}] = 0$. At the R point, the symmetries are $S_{2x} = \{C_{2z}|0, \frac{1}{2}, \frac{1}{2}|\}$, $S_{2x} = \{C_{2z}|\frac{1}{2}, \frac{1}{2}, 0|\}$, and identity operator. The two screws anticommute at the R point. At the X point, the symmetries are $S_{2x} = \{C_{2x}|0, \frac{1}{2}, \frac{1}{2}|\}$ and $S_{2z} = \{C_{2x}|\frac{1}{2}, 0, \frac{1}{2}|\}$.

Let us now understand the emergence of different topological phonon excitations as a function of uniaxial strain. Here we applied a maximum of 3% strain (both in compressive and tensile forms) in an interval of 1% along the c axis. First, we have verified the dynamical stability of the strained systems, and the full phonon spectrum of one of the strained cases (at 3% compressive strain) is displayed in Fig. 5(a). At an ambient state (cubic phase), $KMgBO_3$ hosts two kinds of double Weyl phonons, i.e., spin-1 type at Γ and charge-2 Dirac type at R points. It is clear that, in this strained system, the generators at Γ will enforce the bands to become nondegenerate (since the two screw operators commute), which should destroy the spin-1 type double Weyl phonon nature. The eigenvalues can be ±1 at the Γ point [53]. This is precisely shown in Fig. 5(b) (under 3% compressive strain). The nondegeneracy of bands at the Γ point is also verified from irreducible representation analysis. Coming to the R point, the possible combinations of eigenvalues are (1,−1,−1), (−1,1,−1), (−1,−1,1), and (1,1,1) [53], which provide a fourfold degeneracy and assure the possibility of preserving the charge-2 Dirac point. The bulk phonon dispersion at the R point is shown in Fig. 5(c) (under 3% compressive strain), confirming the persistence of a charge-2 Dirac state at R. To confirm the double Weyl phonon nature, the surface state of a charge-2 Dirac point is simulated, as shown in Fig. 5(d). A highly linearized surface state along with a clear surface arc is visible from this figure.

Further, let us analyze the effect of strain on spin-$\frac{1}{2}$ Weyl phonons. The analysis of band topology between bands 54 and 55 shows the presence of two Weyl points with +1 chirality around the Γ point [with locations (0,0,$+k_z$) and (0,0,$-k_z$)). This balances the chirality generated due to the double Weyl phonons at the R point. Figure 5(e) displays the computed Berry curvature on k_x-k_z plane, which shows the outcome as expected. Importantly, the combination of double and single Weyl phonons conserves the Ninomiya theorem [54] in the strained state. To further understand this point, we have disturbed the symmetry by substituting one of the K elements with Rb. This transforms the system to a low symmetry triclinic space group ($P1$), which lacks all the screw rotation symmetries. To confirm the dynamical stability of the substituted system, we have presented the full phonon spectra of Rb-substituted $KMgBO_3$ in Fig. 5(f). The phonon dispersion of the strained ($P2_12_12_1$) and the substituted phase ($P1$) for a small frequency interval are presented in Figs. 5(g) and 5(h). The Dirac nature at the R point is defaced in the $P1$ phase, which arises purely due to the breaking of screw symmetry, with the simultaneous defacing of +1 chiral Weyl points along $(-Z)$ $-\Gamma - Z$ direction.

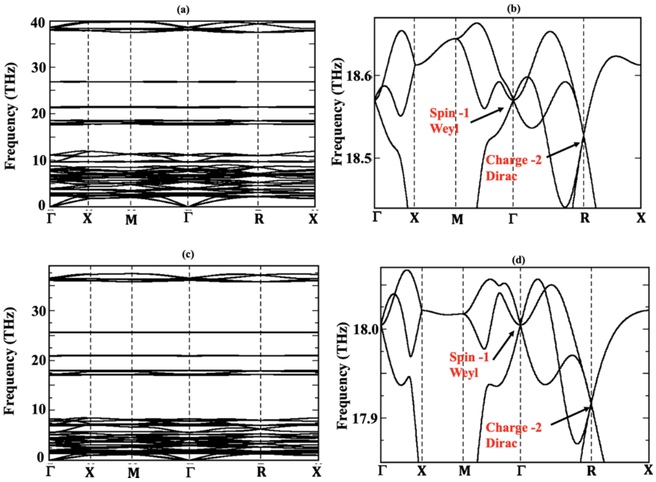

FIG. 6. Full phonon spectra of (a) $RbMgBO_3$ and (c) $CsCdBO_3$. (b), (d) Phonon spectra of $RbMgBO_3$ and $CsCdBO_3$ within a small frequency range indicating the spin-1 Weyl and charge-2 Dirac point nature.

Further, the 1D nodal ring/loop is destroyed under uniaxial strain, with the opening of a gap along Γ-*Y*. Regarding the 2D nodal surface, the presence of screws and time-reversal symmetry induces a Kramers-like double degeneracy at $k_i = \pi$, which causes the formation of a nodal surface. The application of the biaxial strain similarly alters the topological phonon excitations. Changes in other topological features remain in line with those of uniaxial strain.

G. Other materials

We have also analyzed the topological phonon excitations of two other experimentally synthesised prototype compounds, $RbMgBO_3$ and $CsCdBO_3$. Optimized lattice parameters for $RbMgBO_3$ and $CsCdBO_3$ are 7.02 Å and 7.629 Å, respectively, which are in good agreement with the experiment [36,37]. Full phonon spectra confirming the dynamical stability of these compounds are presented in Figs. 6(a) and 6(b). A similar nature of phonon dispersion is observed in these two compounds. They show various topological phonons, including double Weyl, single Weyl, nodal line/loop, and nodal surface. In Figs. 6(c) and 6(d), we have provided the phonon spectra for a small frequency interval, revealing the spin-1 and charge-2 type double Weyl phonon features of $RbMgBO_3$ and $CsCdBO_3$. Corresponding surface spectra on the (001) surface are presented in Figs. 7(a)–7(d). As shown in Figs. 7(a) and 7(c), the spin-1 Weyl points of $RbMgBO_3$ and $CsCdBO_3$ are located around the frequencies around 18.57 THz and 18 THz, respectively. Further, the charge-2 Dirac points are located around 18.53 THz and 17.92 THz for $RbMgBO_3$ and $CsCdBO_3$, respectively. The surface arcs originated from both spin-1 and charge-2 Dirac points are clearly seen from the figures. Overall, the topological features of these compounds are in line with $KMgBO_3$.

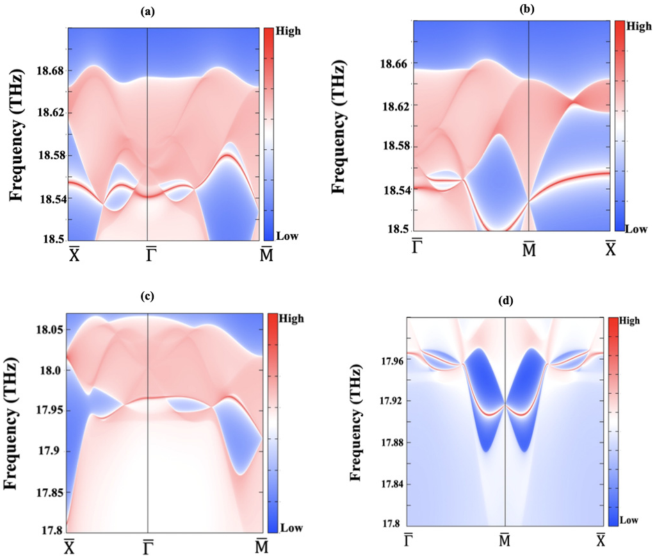

FIG. 7. Surface state around $\bar{\Gamma}$ and $\bar{M}$ point on (001) surface, corresponding to the spin-1 Weyl node and charge-2 Dirac node, respectively, for (a), (b) $RbMgBO_3$ and (c), (d) $CsCdBO_3$.

IV. SUMMARY

We propose three materials ($KMgBO_3$, $RbMgBO_3$, and $CsCdBO_3$) that show topological phonon features in different THz frequency ranges. At ambient conditions, these materials provide a rich platform to simultaneously host several multifold and multidimensional topological Weyl phonons, such as spin-1 Weyl, charge-2 Dirac, single Weyl, nodal line/loop, and nodal surface. These topological states are protected by crystalline and time-reversal symmetries. Application of strain breaks the C_3 rotational symmetry which mediates the elimination of spin-1 double Weyl nodes while preserving the other topological features. Substitution at the K/Rb/Cs site also lowers the symmetry to a triclinic structure and destroys most of the topological features. The present paper showcases a material class where multiple topological phonon excitations coexist and hence can be an interesting platform for future theoretical/experimental investigations.

ACKNOWLEDGMENTS

A.A. acknowledges DST SERB, India (Grant No. CRG/2019/002050) for funding to support this research. S.P.C. thanks IIT Bombay for the institute postdoctoral fellowship and computing facility. C.M. would like to thank Institute for Basic Science in Korea (Grant No. IBS-R009-D1) for funding.

---

[1] K. Manna, Y. Sun, L. Muechler, J. Kübler, and C. Felser, Nat. Rev. Mater. **3**, 244 (2018).

[2] Y. Xia, D. Qian, D. Hsieh, L. Wray, A. Pal, H. Lin, A. Bansil, D. Grauer, Y. S. Hor, R. J. Cava, and M. Z. Hasan, Nat. Phys. **5**, 398 (2009).

[3] S. Wang, B.-C. Lin, A.-Q. Wang, D.-P. Yu, and Z.-M. Liao, Advances in Physics: X **2**, 518 (2017).

[4] H. Zheng and M. Z. Hasan, Advances in Physics X **3**, 1466661 (2018).

[5] M. Sato and Y. Ando, Rep. Prog. Phys. **80**, 076501 (2017).

[6] C.-H. Hsu, P. C. Sreeparvathy, Chanchal K. Barman, F.-C. Chuang, and A. Alam, Phys. Rev. B **103**, 195143 (2021)

[7] Y. Xu, F. Zhang, and C. Zhang, Phys. Rev. Lett. **115**, 265304 (2015)

[8] S. D. Huber, Nat. Phys. **12**, 621 (2016).

[9] R. Süsstrunk and S. D. Huber, Proc. Natl. Acad. Sci. USA **113**, E4767 (2016).

[10] E. Prodan, K. Dobiszewski, A. Kanwal, J. Palmieri, and C. Prodan, Nat. Commun. **8**, 14587 (2017).

[11] T. Zhang, Z. Song, A. Alexandradinata, H. Weng, C. Fang, L. Lu, and Z. Fang, Phys. Rev. Lett. **120**, 016401 (2018).

[12] J. Li, J. Liu, S. A. Baronett, M. Liu, L. Wang, R. Li, Y. Chen, D. Li, Q. Zhu, and X.-Q. Chen, Nat. Commun. **12**, 1204 (2021).

[13] J. Li, Q. Xie, S. Ullah, R. Li, H. Ma, D. Li, Y. Li, and X.-Q. Chen, Phys. Rev. B **97**, 054305 (2018).

[14] Y. Liu, Y. Xu, S.-C. Zhang, and W. Duan, Phys. Rev. B **96**, 064106 (2017).

[15] L. Zhang, J. Ren, J.-S. Wang, and B. Li, Phys. Rev. Lett. **105**, 225901 (2010).

[16] K. Sun, Z. Gao, and J.-S. Wang, Phys. Rev. B **103**, 214301 (2021).

[17] T. Qin, J. Zhou, and J. Shi, Phys. Rev. B **86**, 104305 (2012).

[18] Z. Rao, H. Li, T. Zhang, S. Tian, C. Li, B. Fu, C. Tang, L. Wang, Z. Li, W. Fan, J. Li, Y. Huang, Z. Liu, Y. Long, C. Fang, H. Weng, Y. Shi, H. Lei, Y. Sun, T. Qian, and H. Ding, Nature (London) **567**, 496 (2019).

[19] S.-X. Zhang, S.-K. Jian, and H. Yao, Phys. Rev. B **96**, 241111(R) (2017).

[20] C. K. Barman, C. Mondal, S. Pujari, B. Pathak, and A. Alam, Phys. Rev. B **102**, 155147 (2020).

[21] M. Z. Hasan, G. Chang, I. Belopolski, G. Bian, S.-Y. Xu, J.-X. Yin, Nat. Rev. Mater. **6**, 784 (2021)

[22] X. Wang, Z. Cheng, G. Zhang, B. Wang, X.-L. Wang, and H. Chen, Nanoscale **12**, 8314 (2020)

[23] R. Y. Wang, Z. J. Chen, Z. Q. Huang, B. W. Xia, and H. Xu, Phys. Rev. Materials **5**, 084202 (2021).

[24] C. Xie, Y. Liu, Z. Zhang, F. Zhou, T. Yang, M. Kuang, X. Wang, and G. Zhang, Phys. Rev. B **104**, 045148 (2021).

[25] Y. Jin, R. Wang, and H. Xu, Nano Lett. **18**, 7755 (2018).

[26] T. Yang, C. Xie, H. Chen, X. Wang, and G. Zhang, Phys. Rev. B **105**, 094310 (2022)

[27] S. Singh, Q. Wu, C. Yue, A. H. Romero, and A. A. Soluyanov, Phys. Rev. Materials **2**, 114204 (2018)

[28] J. Wang, H. Yuan, M. Kuang, T. Yang, Z.-M. Yu, Z. Zhang, and X. Wang, Phys. Rev. B **104**, L041107 (2021).

[29] C.-J. Eklund, C. J. Fennie, and K. M. Rabe, Phys. Rev. B **79**, 220101(R) (2009).

[30] L. Jin, X. Zhang, Y. Liu, X. Dai, L. Wang, and G. Liu, Phys. Rev. B **102**, 195104 (2020).

[31] C. Lin, M. Ochi, R. Noguchi, K. Kuroda, M. Sakoda, A. Nomura, M. Tsubota, P. Zhang, C. Bareille, K. Kurokawa, Y. Arai, K. Kawaguchi, H. Tanaka, K. Yaji, A. Harasawa, M. Hashimoto, D. Lu, S. Shin, R. Arita, S. Tanda, and T. Kondo, Nat. Mater. **20**, 1093 (2021).

[32] S. M. Young, S. Chowdhury, E. J. Walter, E. J. Mele, C. L. Kane, and A. M. Rappe, Phys. Rev. B **84**, 085106 (2011).

[33] Y. Sun, S.-C. Wu, M. N. Ali, C. Felser, and B. Yan, Phys. Rev. B **92**, 161107(R) (2015).

[34] L. Wu, J. C. Sun, Y. Zhang, S. F. Jin, Y. F. Kong, and J. J. Xu, Inorg. Chem. **49**, 2715 (2010).

[35] J. Zheng, Q. Cheng, S. Wu, Y. Zhuang, Z. Guo, Y. Lu, and C. Chen, Mater. Chem. Phys. **165**, 168 (2015).

[36] R. V. Kurbatov, Leonid A. Solovyov, B. G. Bazarov, A. K. Subanakov, and J. G. Bazarova, Solid State Commun. **172**, 33 (2013).

[37] H. Yu, H. Wu, S. Pan, B. Zhang, M. Wen, Z. Yang, H. Li, and X. Jiang, Eur. J. Inorg. Chem. **2013**, 5528 (2013).

[38] G. Kresse and J. Hafner, Phys. Rev. B **47**, 558(R) (1993).

[39] G. Kresse and D. Joubert, Phys. Rev. B **59**, 1758 (1999).

[40] A. Togo and I. Tanaka, Scr. Mater. **108**, 1 (2015).

[41] Q. Wu, S. Zhang, H.-F. Song, M. Troyer, and A. A. Soluyanov, Comput. Phys. Commun. **224**, 405 (2018).

[42] J. Gao, Q. Wu, C. Persson, and Z. Wang, Comput. Phys. Commun. **261**, 107760 (2021)

[43] P. Cracknell and C. J. Bradley, *The Mathematical Theory of Symmetry in Solids: Representation Theory for Point Groups and Space Groups* (Clarendon Press, Oxford, 1972).

[44] B. Bradlyn, J. Cano, Z. Wang, M. G. Vergniory, C. Felser, R. J. Cava, and B. A. Bernevig, Science **353**, aaf5037 (2016).

[45] The general definition of the type-I and type-II Weyl nodes in a fermionic systems can be understood the following way: The Weyl point, which possesses a zerolike Fermi surface, is defined as type I, and type II shows a tilted dispersion along the momentum space and makes an overlap between the electron and hole pockets [46]. A phonon counterpart for both type I and type II can be understood in a similar way [47].

[46] A. A. Soluyanov, D. Gresch, Z. Wang, Q. Wu, M. Troyer, X. Dai, and B. A. Bernevig, Nature (London) **527**, 495 (2015).

[47] B. W. Xia, R. Wang, Z. J. Chen, Y. J. Zhao, and H. Xu, Phys. Rev. Lett. **123**, 065501 (2019).

[48] J.-Y. You, X.-L. Sheng, G. Su, Phys. Rev. B **103**, 165143 (2021).

[49] Q.-B. Liu, Z.-Q. Wang, and H.-H. Fu, Phys. Rev. B **104**, L041405 (2021).

[50] Y. Yang, J.-P. Xia, H.-X. Sun, Y. Ge, D. Jia, S.-Q. Yuan, S. A. Yang, Y. Chong, and B. Zhang, Nat. Commun. **10**, 5185 (2019).

[51] The combination of twofold screw rotational symmetry and the time-reversal symmetry operators leads to the formation of an antiunitary operator $(TC_{2i})^2 = -1$, which opens up the possibility of a higher dimensional (2D) band degeneracy at $k_i = \pi$ plane. As a result of $(TC_{2i})^2 = -1$, at $k_i = \pi$ high symmetry plane the bands act like Kramers degenerate with eigenvalue ±i.

[52] X. Wang, F. Zhou, T. Yang, M. Kuang, Z.-M. Yu, and G. Zhang, Phys. Rev. B **104**, L041104 (2021)

[53] R. M. Geilhufe, S. S. Borysov, A. Bouhon and A. V. Balatsky, Sci. Rep. **7**, 7298 (2017).

[54] H. B. Nielsen and M. Ninomiya, Phys. Lett. B **105**, 219 (1981).